CONEM 2016 CONGRESSO NACIONAL DE ENGENHARIA MECÂNICA

ABCM 40 anos Associação Brasileira de Engenharia e Ciências Mecânicas

21 - 25 AGOSTO DE 2016 FORTALEZA - CEARÁ

THERMAL ANALYSIS OF THE BRAZILIAN 14-X HYPERSONIC AEROSPACE VEHICLE AT MACH NUMBER 7

Felipe Jean da Costa, felipejean@ieav.cta.br[1]
Israel da Silveira Rêgo, israel.rego@ieav.cta.br[2]
Marco Antônio Sala Minucci, marco.salaminucci@gmail.com[2]
Paulo Gilberto de Paula Toro, toro@ieav.cta.br[2]

[1]ITA - Instituto Tecnológico de Aeronáutica, Praça Marechal Eduardo Gomes, nº 50 Vila das Acácias CEP. 12.228-900 São José dos Campos, SP - Brasil
[2]IEAv - Instituto de Estudos Avançados, Trevo Coronel Aviador José Alberto Albano do Amarante, nº 1 Putim CEP. 12.228-001 São José dos Campos, SP - Brasil

Abstract: *The Brazilian 14-X Hypersonic Aerospace Vehicle, designed at the Prof. Henry T. Nagamatsu Laboratory of Aerothermodynamics and Hypersonics, at the Institute for Advanced Studies, is a technological demonstrator endowed with two innovative technologies: waverider technology, to obtain lift from conical shockwave during the hypersonic flight; and hypersonic airbreathing propulsion system based on supersonic combustion (scramjet), to fly at Earth's atmosphere at 30 km altitude at Mach numbers 7 and 10. Basically, scramjet is an aeronautical engine without moving parts that uses the conical/oblique shockwaves generated during the hypersonic flight, to promote compression and deceleration of freestream atmospheric air at the inlet of the scramjet. On the understanding of the aerodynamic heating it is important to analyze the heat conduction transfer to the 14-X waverider internal structure. ANSYS Workbench software provides the Thermal Numerical Analysis, using Finite Element Method of the 14-X waverider unpowered scramjet at 30 km altitude at Mach number 7 and 10 in terms of temperature and heat flux. Finally, it's possible to verify if the internal temperature comply with the requirements for embedded systems, and, if is necessary to do modifications on the structure in terms of wall thickness and materials.*

keywords: *scramjet, 14-X, Hypersonics, Thermal Analisys, Finite Element Method*

1. THE BRAZILIAN 14-X HYPERSONIC AEROSPACE VEHICLE

The Prof. Henry T. Nagamatsu Laboratory of Aerothermodynamics and Hypersonics, at the Institute for Advanced Studies, is developing the 14-X Hypersonic Aerospace Vehicle, 14-X waverider (Figure 1). The 14-X waverider is a technological demonstrator designed to demonstrate, during the hypersonic flight speed corresponding to Mach number 10 through the Earth's atmosphere at 30 km altitude, endowed of two innovative technologies: waverider technology, to obtain lift from conical shockwave during the supersonic or hypersonic flight; and the scramjet engine that consists in a hypersonic airbreathing propulsion system based on supersonic combustion (Costa, 2014).

Scramjet engine uses the oblique/conical shockwaves generated during the hypersonic flight, to promote compression and deceleration of freestream atmospheric air at the inlet of the scramjet integrated to the vehicle to obtain the air in supersonic speed conditions to burn fuel (in general, hydrogen) in the combustion chamber. Due to the fact that the scramjet engine does not have moving parts, it is necessary another propulsion system to accelerate the vehicle powered by scramjet up to operation conditions. Rocket engines are low-cost solution to launch the powered vehicle by scramjet to the flight test conditions. The Brazilian two-stage rocket engines (S31 and S30) are able to boost the VHA 14-X to the predetermined conditions of the operation of the scramjet at 30 km altitude, but at Mach number 7 (the maximum corresponding speed that S31 and S30 reaches).

Hypersonic flight introduces extreme thermal loads on the leading edges of the vehicle, which generates high temperature around the vehicle surfaces. Consequently, high temperature materials and high temperature coatings should be employed, as carbon-carbon, Inconel 718 and tungsten, that have particularly structural, aerodynamic and thermal protection function (Harsha *et al.*, 2005). The extreme thermal loads on the leading edges of the vehicle have a significant magnitude in terms of heat flux. The heat flux increases inversely to the square root of the nose radius, as says the stagnation heat transfer theory, developed by Fay and Riddell (Glass, 2008).

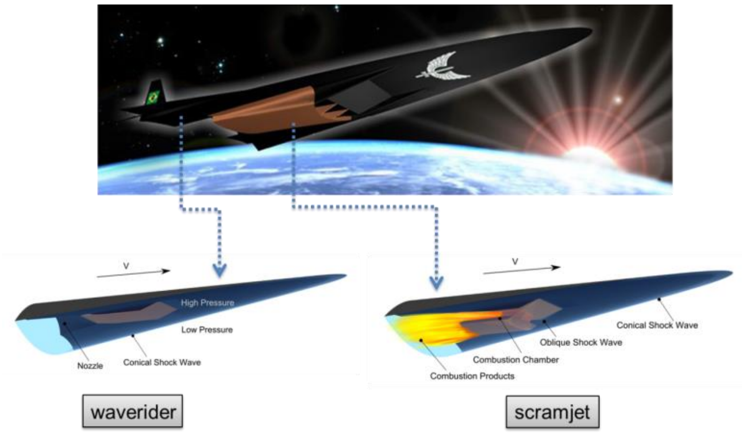

Figure 1. The 14-X Hypersonic Aerospace Vehicle with waverider and scramjet concepts (Costa, 2014).

The 2-m long 14-X Hypersonic Mach number 10 Aerospace Vehicle (Figure 2) was designed to flight at 30 km altitude at Mach number 10 for the first time, in Brazil, based on waverider (Rolim, 2009; Rolim *et al.*, 2009; Rolim *et al.*, 2011) and scramjet engine (Moura, 2009) experimental data as well as on the one-dimensional theoretical analysis, based on conical and oblique compressible flow (Anderson, 2003) and Prandtl-Meyer expansion flow (Anderson, 2003) theories, applied to the external and internal compression surfaces and to the internal and external expansion surfaces, respectively.

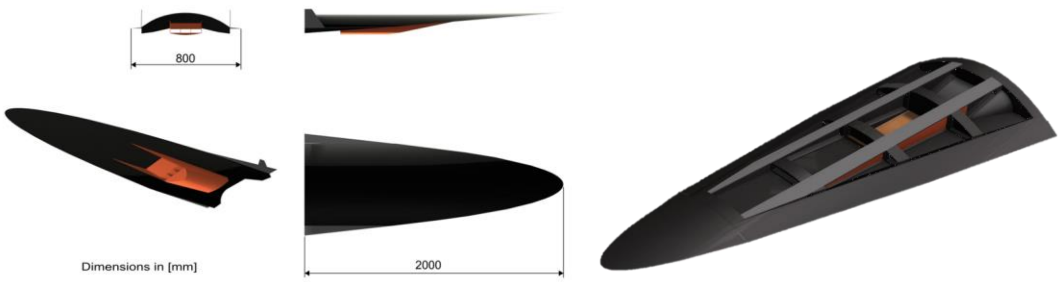

Figure 2. Dimensions and internal configuration of the 14-X Hypersonic Aerospace Vehicle, adapted from Costa (2011).

The internal layout of VHA 14-X (Figure 2) follows the typically aeronautical structure presented by the X-43 A vehicle. Further, the structural analysis will be performed based on the thermodynamic properties obtained from the analytical and experimental data of the waverider and the scramjet configurations, the dynamic pressure at 30 km altitude, the subsystems on-board of the 14-X, the materials available in Brazil, and the internal configuration (Figure 3) developed preliminarily for the internal structure with three ribs and three stringers with slots (Costa, 2011). Should be mentioned the structural materials, specified for the VHA 14-X, are available in Brazil and they are used at the Brazilian VSB-30 (Heitkoetter *et al.*, 2009). Based in this scenario, the structural materials to be used for the VHA 14-X (Figure 3), are the special steel 4140 for the stringers, the stainless steel 304 for the ribs, the tungsten to the conical nose, the Carbon-Carbon (C-C) for the leading edges and for the passive thermal protection system (all skins) and Inconel 718 for the scramjet engine (Costa, 2011).

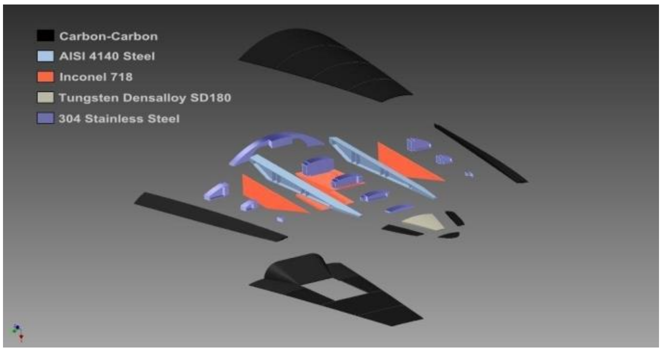

Figure 3. VHA 14-X material specification and layout, adapted from, adapted from Costa (2011).

2. THERMAL ANALYSIS

2.1. Mesh generation and convergence

The mesh generated by ANSYS Workbench (automatically) for the VHA 14-X showed the presence of degenerate elements, which it is characteristic of non-structured mesh, and can generate results that do not match reality. Appropriate tools of the software ANSYS Workbench were used for structure the mesh, such as element sizing, number of division, method, etc. The optimized mesh (Figure 4) containing 184632 nodes and 61619 elements (hexahedral and tetrahedral) was obtained using the geometry of VHA 14-X waverider implemented in the software ANSYS.

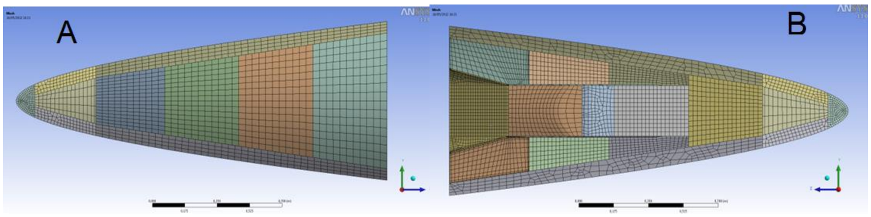

Figure 4. VHA 14-X treated mesh (Costa *et al.*, 2013).

In the numerical analysis the mesh element type is very important due to the formulation and the physical application type, and in the present case is used the SOLID186 (Figure 4 a) and SOLID187 (Figure 4 b) from the ANSYS Workbench 14.5. The SOLID186 presents a quadratic displacement behavior and it is a higher order 3-D 20-node solid element. The element is defined by 20 nodes with three degrees of freedom per node and the nodal translations in the x, y, and z directions. The element SOLID187 allows plasticity, stress stiffening, creep, hyperelasticity, large deflection, and large strain capabilities. The formulation includes mixed capability for simulating deformations of nearly incompressible elastoplastic materials, and fully incompressible hyperelastic materials. An alternative with low order precision version is to use the SOLID185. The element geometry is defined by 10 nodes, three degrees of freedom per node and translations in x, y, and z directions. The element capabilities comprise plasticity, hyperelasticity, creep, stress stiffening, large deflection, and large strain. For simulating deformations of nearly incompressible elastoplastic materials, and fully incompressible hyperelastic materials, the SOLID187 element uses the mixed formulation.

2.2. Heat transfer

Heat transfer may occur in one or more of its three basic forms: conduction, convection, and radiation. The Fourier heat conduction law states that the heat flow is proportional to the temperature gradient (Reddy and Gartling, 2010). Convection heat is the energy transport affected by the motion of a fluid. Newton's law of cooling governs the convection heat transfer between two dissimilar media. For convection the heat flow is proportional to the difference of the temperatures of two media. Convection heat transfer coefficient or film conductance is the proportionality constant (Reddy and Gartling, 2010). The radiant or electromagnetic energy emitted by a medium is unique to the temperature of the medium; this is defined as thermal radiation. The Stefan-Boltzmann law describes the radiant exchange between surfaces or region, and the radiant energy transmitted is proportional to the difference of fourth power of the temperatures of the surfaces, this proportional parameter is called Stefan-Boltzmann constant (Reddy and Gartling, 2010). The Laplace equation (Ho, 2010) is the three-dimensional flow governing equation of heat into a solid in steady-state. It can be used to describe the thermal response of the structure. For 3-D Conduction Heat Transfer is given by:

$$\frac{\partial}{\partial x}\left(k\frac{\partial t}{\partial x}\right)+\frac{\partial}{\partial y}\left(k\frac{\partial t}{\partial y}\right)+\frac{\partial}{\partial z}\left(k\frac{\partial t}{\partial z}\right)-\rho cp\frac{\partial T}{\partial t}=0 \quad (1)$$

where, ρ is the density, c_p is specific heat at constant pressure of the solid, k is thermal conductivity of the solid and T is the conduction heat flux in the *x, y* and *z* directions, respectively.

2.3. Finite element method in heat transfer

The finite element equations may be derivate using the principles of virtual work or minimum potential energy. However, despite these methods are powerful, they require more knowledge in structural mechanics than we need. The adopted approach to derive equations for the finite element method relies on the method of weighted residuals that is able to thermal and structural problems. Furthermore, we have a mathematical equivalence between method of weighted residuals and principles of virtual work, that both derive the same equations, but the first method requires no background in energy methods (Thornton, 1996). We assume general boundary conditions so that a variety of heat sources and losses may be simulated, and the temperature-dependent properties and radiation exchanges may occur, becoming a non-linear problem. The main objective is to evaluate the temperature field *T (x, y, z, t)* throughout the aerospace vehicle structure, that followed by a structural analysis may provide detailed deformations and stresses (Thornton, 1996). Figure 5 shows three-dimensional heat transfer in an anisotropic structure Ω with a surface Γ as boundary. Considering the conservation of energy equation:

$$-\left(\frac{\partial q_x}{\partial x}+\frac{\partial q_y}{\partial y}+\frac{\partial q_z}{\partial z}\right)+Q=\rho cp\frac{\partial T}{\partial t} \tag{2}$$

where, q_x, q_y, q_z are the conduction heat fluxes, *Q (x, y, z, t)* is the internal heat generation rate per volume unit, ρ is the density, and *c* is the specific heat. Adapting the Fourier's law for anisotropic material, we can write:

$$\begin{aligned} q_x &= -\left(k_{11}\frac{\partial T}{\partial x}+k_{12}\frac{\partial T}{\partial y}+k_{13}\frac{\partial T}{\partial z}\right)\\ q_y &= -\left(k_{21}\frac{\partial T}{\partial x}+k_{22}\frac{\partial T}{\partial y}+k_{23}\frac{\partial T}{\partial z}\right)\\ q_z &= -\left(k_{31}\frac{\partial T}{\partial x}+k_{32}\frac{\partial T}{\partial y}+k_{33}\frac{\partial T}{\partial z}\right) \end{aligned} \tag{3}$$

where, k_{ij} is the symmetric thermal-conductivity tensor.

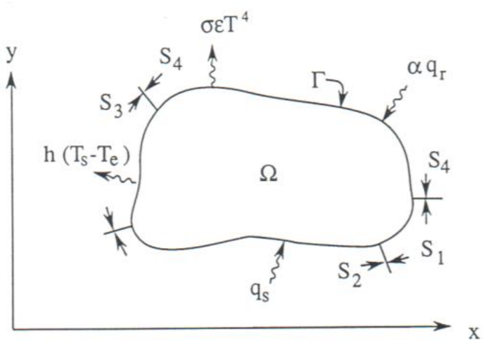

Figure 5. Heat transfer in an anisotropic structure (Thornton, 1996).

Applying boundary conditions on all portions of the surface Γ and an initial condition the heat conduction equations can be solved. The boundary conditions for heat conduction take several forms, like prescribed surface temperature, prescribed surface heat flux, convective heat exchange and radiation exchange. Bellow follows the boundary conditions:

$$T_s = T_s(x,y,z,t) \quad \text{on } S_1 \tag{4}$$
$$q_n = -q_s \quad \text{on } S_2 \tag{5}$$
$$q_n = h(T_s - T_e) \quad \text{on } S_3 \tag{6}$$
$$q_n = \sigma\varepsilon T_s^4 - \alpha q_R \quad \text{on } S_4 \tag{7}$$

where, T_s is the specified surface temperature, q_n represents the heat flux normal to the surface, q_s is the specified surface heat flux (positive into the surface), h is the convective heat transfer coefficient, T_e is the convective exchange temperature, σ is the Stefan-Boltzmann constant, ε is the surface emissivity, α is the surface absorptivity, and q_R is the incident radiation heat flux.

For the solution of finite element equations, we need to divide the domain Ω (Figure 13) into M elements of r nodes each. The temperature and temperature gradients are expressed by:

$$T(x, y, z, t) = [N(x, y, z)]\{T(t)\} \tag{8}$$

and

$$\begin{Bmatrix} \frac{\partial T}{\partial x}(x, y, z, t) \\ \frac{\partial T}{\partial y}(x, y, z, t) \\ \frac{\partial T}{\partial z}(x, y, z, t) \end{Bmatrix} = [B(x, y, z)]\{T(t)\} \tag{9}$$

where, *[N]* is the temperature interpolation matrix, *[B]* the temperature gradient interpolation matrix, and *{T}* the vector of nodal temperatures. The temperature interpolation matrix is a row matrix of the interpolation functions,

$$[N] = [N_1 \quad N_2 \quad \ldots \quad N_r] \tag{10}$$

The temperature gradient interpolation matrix is a rectangular array of interpolation function derivatives.

$$[B] = \begin{bmatrix} \frac{\partial N_1}{\partial x} & \frac{\partial N_2}{\partial x} & \cdots & \frac{\partial N_2}{\partial x} \\ \frac{\partial N_1}{\partial y} & \frac{\partial N_2}{\partial y} & \cdots & \frac{\partial N_2}{\partial y} \\ \frac{\partial N_1}{\partial z} & \frac{\partial N_2}{\partial z} & \cdots & \frac{\partial N_2}{\partial z} \end{bmatrix} \tag{11}$$

Using the Method of Weighted Residuals (MWR) to derive the element equations, we satisfy the equation of energy conservation for each element that represents the energy balance of the element. Firstly, we need to change the temperature representation substituting the Eq. 8 into the Eq. 2 to satisfy exactly the conservation of energy, resulting in a residual function. Considering the MWR and multiplying the residual by a weighting function interpolation functions $N_i, i = 1,2,\ldots,r$, and integrate the weighted residual over the solution domain Ω_e as follow:

$$\int \Omega_e \left(\frac{\partial q_x}{\partial x} + \frac{\partial q_y}{\partial y} + \frac{\partial q_z}{\partial z} - Q + \rho c \frac{\partial T}{\partial t} \right) N_i d\Omega = 0 \qquad i = 1,2,\ldots,r \tag{12}$$

Equation 12 represents, for an element, r equations for r nodal temperatures. The next step is integrate the derivative heat fluxes by parts using Gauss's theorem to introduce on the boundary element a surface integral, which sum of integrals over S_1, S_2, S_3 and S_4 of the surface, where the boundary conditions are applied. Writing the results of the integration by parts we have:

$$\int \Omega_e \rho c \frac{\partial T}{\partial t} N_i d\Omega - \int \Omega_e \begin{bmatrix} \frac{\partial N_i}{\partial x} & \frac{\partial N_i}{\partial y} & \frac{\partial N_i}{\partial z} \end{bmatrix} \begin{Bmatrix} q_x \\ q_y \\ q_z \end{Bmatrix} d\Omega = \int \Omega_e Q N_i d\Omega - \int S_1 (\vec{q} \cdot \hat{n}) N_i dS +$$
$$\int S_2 q_S N_i ds - \int S_3 h(T - T_e) N_i dS - \int S_4 (\sigma \varepsilon T^4 - \alpha q_r) N_i dS \qquad i = 1,2,\ldots,r \tag{13}$$

where, $\vec{q} = q_x \hat{i} + q_y \hat{j} + q_z \hat{k}$ is the heat-flux vector, and is $\hat{n}$ a unit normal vector to the surface. Introducing the interpolations for the element temperature and heat-flux components we can write the heat fluxes from the Fourier's law (Eq. 2) in matrix form:

$$\begin{Bmatrix} q_x \\ q_y \\ q_z \end{Bmatrix} = -[k] \begin{Bmatrix} \frac{\partial T}{\partial x} \\ \frac{\partial T}{\partial y} \\ \frac{\partial T}{\partial z} \end{Bmatrix}$$

Using Eq.108 we eliminate the temperature gradients, thus we have:

$$\begin{Bmatrix} q_x \\ q_y \\ q_z \end{Bmatrix} = -[k][B]\{T\} \tag{14}$$

Inserting the Eqs. 11 and 14 into the Eq. 13 we can write:

$$[C]\{\dot{T}\} + [[k_c] + [k_h]]\{T\} = \{R_T\} + \{R_Q\} + \{R_q\} + \{R_h\} + \{R_\sigma\} + \{R_R\} \tag{15}$$

where, $[C]$ is the element capacitance matrix, $[k_C]$ and $[k_h]$ are the element conductance matrices and relate to conduction and surface convection, respectively. The vector $\{R_T\}$ corresponds to the nodal heat flow, but generally this vector is not computed because the nodal temperature is specified when we solve the global equations. The vectors $\{R_Q\}$, $\{R_q\}$, and $\{R_h\}$ represent the element heat load vectors in terms of internal heat generation, surface heating, and surface convection. The last two vectors $\{R_\sigma\}$ and $\{R_R\}$ are used for emitted and absorbed radiation, respectively.

Coupling the matrices defined in Eq. 15 to the global equations form, we have:

$$[C(T,t)]\{\dot{T}\} + [k(T,t)]\{T\} = \{R(R,t)\} \tag{16}$$

where, $[C(T,t)]$ is the global capacitance matrix, $[K(T,t)]$ the global conductance matrix, and $\{R(T,t)\}$ is the global load vector, that may be temperature and time-dependent.

Equation 16 corresponds to a set of simultaneous, first-order, nonlinear ordinary differential equations for transient problem. For steady-state problems we may rewrite the Eq. 16 as:

$$\{F(T)\} = [k(T)]\{T\} - \{R(T)\} \tag{17}$$

where, the vector $\{F(T)\}$ is the unbalance, or residual, for an approximate solution vector $\{T\}$ in the equations.

2.4. Material data

The temperature distribution may affect appreciably the material properties such as modulus of elasticity and the coefficient of thermal expansion (CTE). For the finite element analysis we need to accommodate the temperature dependent properties that are based on the element average temperature and assumed constant within an element. To consider temperature dependent properties we need a material database from a thermo-structural characterization, and thus, for the materials used for the VHA 14-X. The access for this database has several difficulties, fact for which we chose to use the constant material properties according to supplier datasheets and are presented in tables 1 and 2.

Table 1. Thermal properties of isotropic materials (Costa, 2014).

MATERIAL	CTE [μm/ m-°C]	Specific Heat Capacity [J/g-°C]	Thermal Conductivity [W/m-K]	Melting Point [°C]	Emissivity
Steel 4140	14.6	0.561	33.0	-	-
Stainless Steel 304	18.7	0.500	21.5	1400 - 1455	-
Inconel 718	13.0	0.435	11.4	1260 - 1336	0.85
Tungsten	4.40	0.134	117	3370	0.15

Table 2. Thermal properties of orthotropic material, C-C (Costa, 2014).

MATERIAL	CTE [µm/ m-°C]	Thermal Conductivity [W/m-K]	Emissivity
***x*-direction**	1.06E-06	11.5	0.95
***y*-direction**	1.06E-06	11.5	0.95
***z*-direction**	9.9E-07	11.6	0.95

2.5. Boundary conditions

The boundary conditions used for steady-state analysis are the aerodynamic heating (Costa, 2014) from the Fay and Riddell (Table 3) and Eckert (Tables 4-6) theories, that provide the heat flux over the vehicle surface, divided into 11 regions (Figure 6). Thus, was applied the heat flux, from Fay and Riddell method, on the stagnation point along of the VHA 14-X leading edge and the heat flux, by Eckert reference enthalpy, over the all external surface of VHA 14-X. Figure 7 present the boundary conditions applied to the lower and upper surfaces of the VHA 14-X, respectively. The radiation condition considers the emissivity according to Table 2, and the local temperature for which altitude.

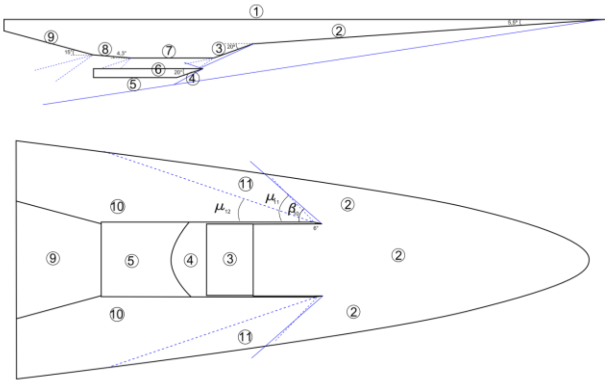

Figure 6. VHA 14-X arbitrary regions for Analytical Theoretical Analysis.

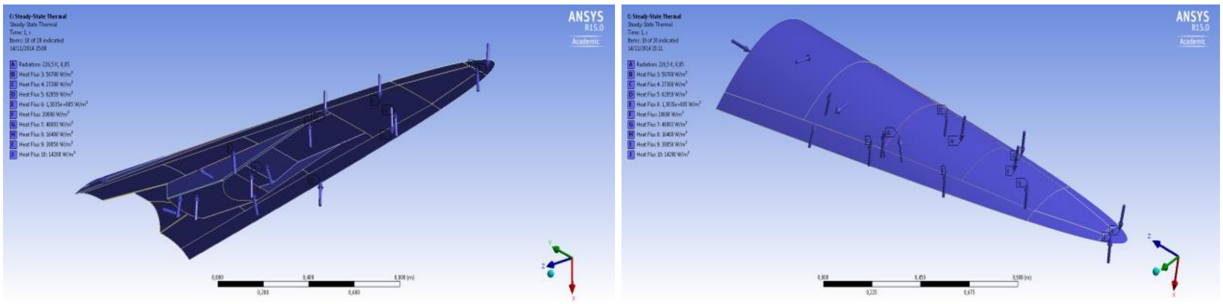

Figure 7. Heat flux and radiation applied to the lower and upper surfaces of the VHA 14-X.

Table 3. Heat Flux at Stagnation Point (Costa, 2014).

Mach number	Heat flux [W/m²]
7	692,345.3238

Table 4. Heat flux by coordinates in region 1 of the VHA 14-X vehicle (Costa, 2014).

q_1 [W/m²]	Coordinates					
Mach	**0.1**	**0.43**	**0.8**	**1.2**	**1.6**	**2**
7	47061.6	22695.1	16638.7	13585.5	11765.4	10523.2

Table 5. Heat flux by coordinates in region 2 of the VHA 14-X vehicle (Costa, 2014).

q_1 [W/m²]	Coordinates			
Mach	**0.1**	**0.43**	**0.8**	**1.17295**
7	58202.5	28066.8	20576.1	16992.1

Table 6. Heat flux over the VHA 14-X vehicle regions (Costa, 2014).

Mach	$q_{3,4}$ [W/m²]	q_5 [W/m²]	$q_{6,7}$ [W/m²]	q_8 [W/m²]	q_9 [W/m²]	q_{10} [W/m²]	q_{11} [W/m²]
7	115021	176595	103744.4	125358.4	57325.7	165383.9	18645.2

3. RESULTS

3.1. Thermal analysis

The heat fluxes and radiation are applied to the external surfaces, and at internal surfaces we do apply the adiabatic wall boundary condition to analyze the heat transfer for the internal structure. Figure 8 shows the temperature field over the lower surface, internal structure and upper surface for the VHA 14-X at Mach number 7 with Carbon-Carbon skins. In this context, the maximum temperature of 1397.6 K occurs at the stagnation point of the leading edge (Fig. 8). The scramjet engine presents a temperature field near to the maximum temperature. The minimum temperature occurs at the trailing edge of the VHA 14-X with value of 571.57 K.

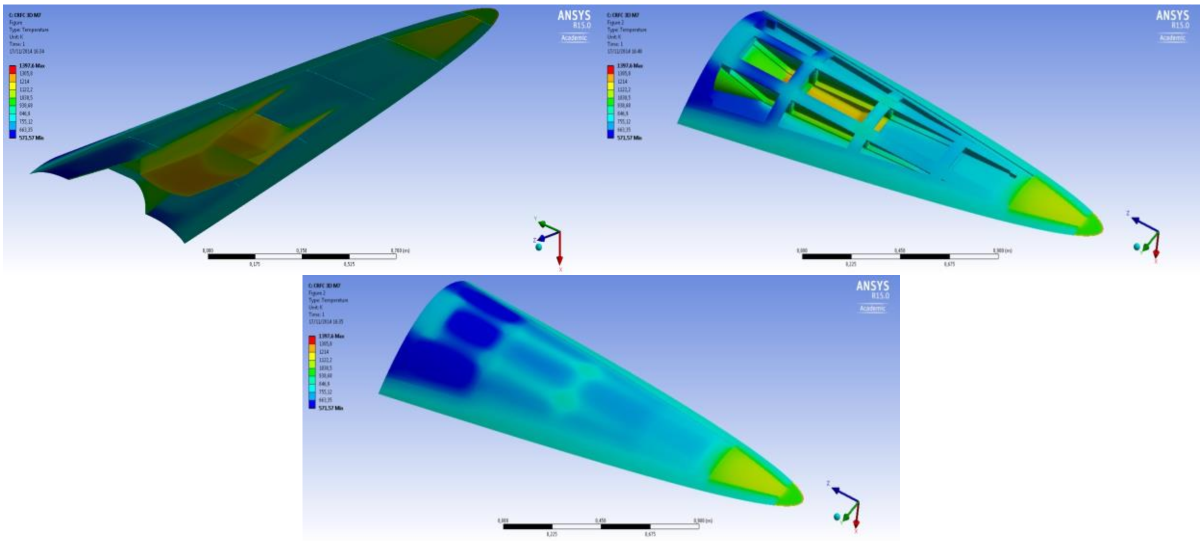

Figure 8. Temperature field over the internal and external structure of the VHA 14-X at Mach number 7 with C-C 3D skins.

We can obtain the total heat flux over the VHA 14-X at Mach number 7 with Carbon-Carbon 3D skins, as shown in Figure 9, with maximum value of 1.3802 106 W/m² at the regions near to the leading edge and minimum of 15.553 W/m² along of the vehicle.

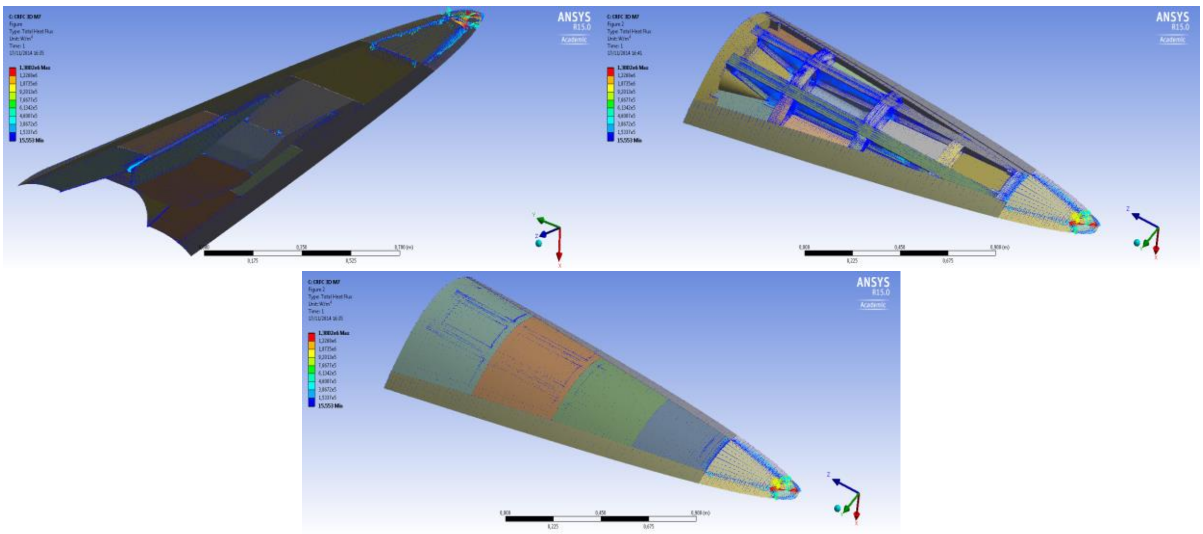

Figure 9. Total heat flux over the internal and external structure of the VHA 14-X at Mach number 7 with C-C 3D skins.

3.2. Thermal analysis for Inconel 718

Now, we will consider the VHA 14-X flying at Mach number 7 with Inconel 718 as skin material, and the temperature field is presented in Figure 10 over the lower surface, internal structure and upper surface, respectively. In this situation the maximum temperature of 1394.8 K occurs at the stagnation point of the leading edge and in the scramjet engine presents a field of temperatures near to the maximum temperature. The minimum temperature occurs along of the vehicle with value of 696.13 K.

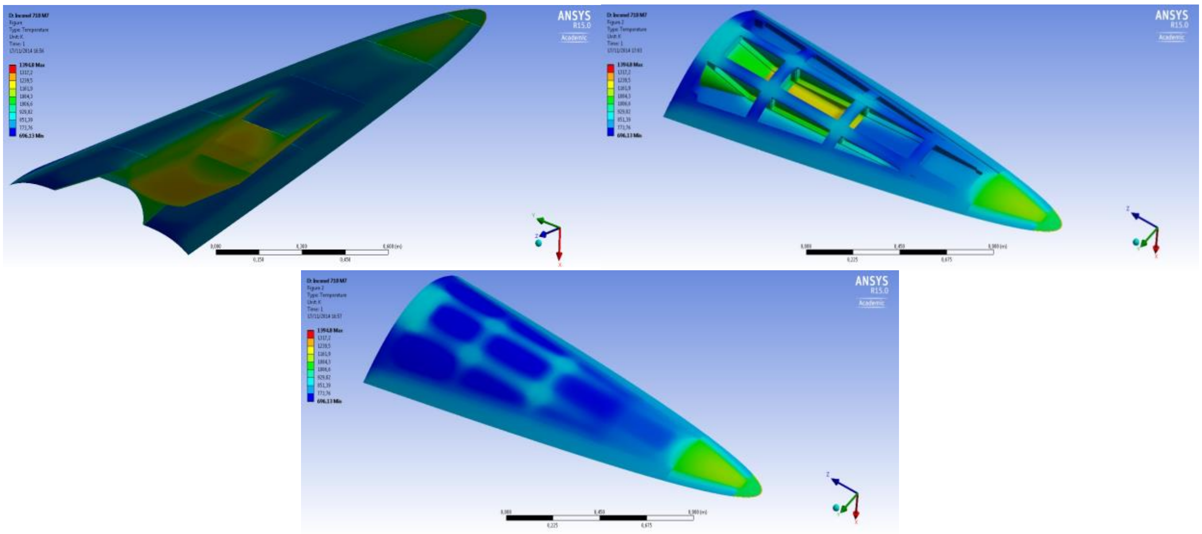

Figure 10. Temperature field over the internal and external structure of the VHA 14-X at Mach number 7 with Inconel skins.

The total heat flux over the VHA 14-X at Mach number 7 with Inconel 718 skins, is showed in Figure 11, over the lower surface, internal structure and upper surface, respectively. The maximum value of 1.38 106 W/m^2 at the regions near to the leading edge and minimum of 16.02 W/m^2 along the vehicle.

Table 7 summarizes the maximum values of the all thermal results. Note that the thermal behavior of VHA 14-X structure has a small difference between the two materials considerate in this analysis.

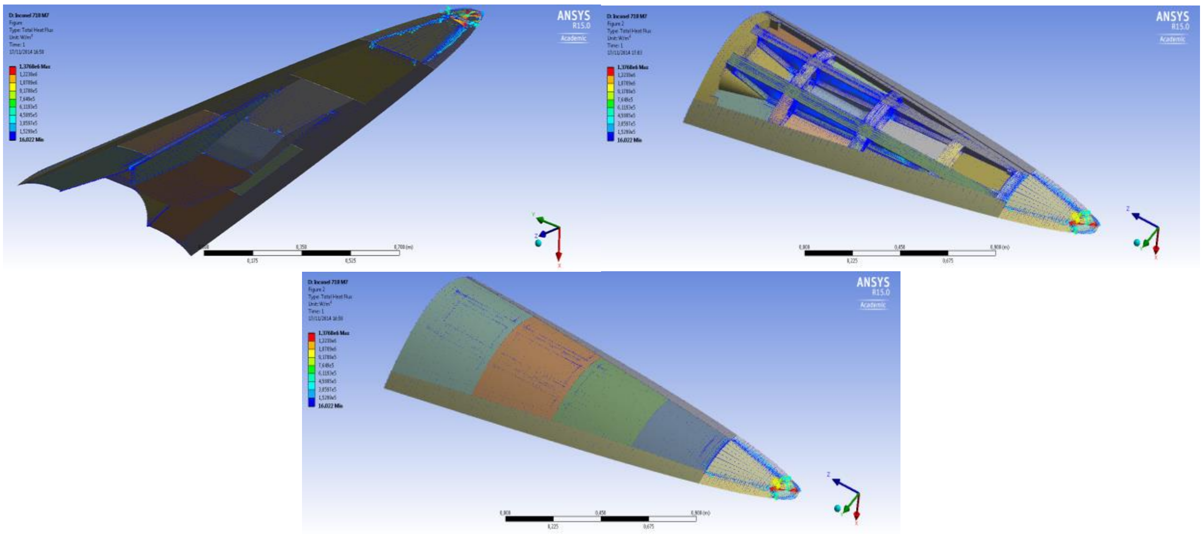

Figure 11. Temperature field over the internal and external structure of the VHA 14-X at Mach number 7 with Inconel skins.

Table 7. Thermal Response comparison between C-C and Inconel 718 skins.

Skin Material	Carbon-Carbon 3D	Inconel 718	Comparison %
Temperature [K]	1397.6	1394.8	0.00200
Total Heat Flux [W/m^2]	$1.38x10^6$	$1.38x10^6$	0.00246

4. CONCLUSION

Based on the aerodynamic heating data (Costa, 2014), TPS and structural material thermal properties (Costa, 2014), 14-X waverider design (Costa, 2011), we presented on this work the thermal analysis (heat flux and temperature) considering two alternatives for the skin material (C-C and Inconel 718) of the 14-X waverider, and which the flight test will occur at 30 km altitude with speed corresponding to Mach number 7.

ANSYS Workbench software provided the Thermal Numerical Analysis using Finite Element Method, and showed that we have a small difference in terms of thermal response considering C-C and Inconel 718 as skin material of the 14-X waverider. Also, in the future works, is necessary to keep attention for the scramjet engine, due the high temperature gradients, requiring the application of additional thermal protection system.

5. ACKNOWLEDGMENTS

The last author would like to express gratitude to FINEP (project nº 0445/07), to CNPq (project nº 471345/2007-5) and to AEB (project nº 25/2009-1) for the financial support for the 14-X Hypersonic Aerospace Vehicle design and experimental investigations.

6. REFERENCES

Anderson JR., J. D. Modern Compressible Flow, with Historical Perspective. 3ª ed. McGraw-Hill, 2003.

Ansys. Help. 2012.

Costa, F.J., 2011, Projeto Dimensional para Manufatura do Veículo Hipersônico Aeroespacial 14-X (in Portuguese). Undergraduate Work, FATEC de São José dos Campos: Professor Jessen Vidal, Brazil.

Costa, F. J. ; Toro, P. G. P. ; Rolim, T. C. ; Camillo, G. P. Brazilian 14-X Hypersonic Waverider Unpowered Scramjet Aerospace Vehicle Structural Analysis At Mach Number 7. In: COBEM- 22nd International Congress of Mechanical Engineering, 2013, Ribeirão Preto.

Costa, F. J., Thermo-Structural Analysis of the Brazilian 14-X Hypersonic Aerospace Vehicle. 2014. 195 p. Dissertation of Master in Science. Instituto Tecnológico de Aeronáutica, São José dos Campos, Brasil.

Glass, D. E. Ceramic Matrix Composite (CMC) Thermal Protection Systems (TPS) and Hot Structures for Hypersonic Vehicles. In: 15th AIAA International Space Planes and Hypersonic Systems and Technologies Conference, 28 April - 1 May 2008 (AIAA 2008-2682), Dayton, Ohio – USA.

Hankey, W. L. Re-Entry Aerodynamics. AIAA Education Series, J.S. Przemieniecki, Series Editor-in-Chief, 1988, AIAA, ISBN 978-0-930403-33-1.

Harsha, P. T., Keel, L. C., Castrogiovanni, E. A. e Sherrill, R. T. X-43A Vehicle Design and Manufacture. In: AIAA/CIRA 13th International Space Planes and Hypersonic Systems and Technologies Conference, 2005 (AIAA 2005-3334), Capua, Italia.

Heitkoetter, R. F.; Almeida, S. F. M. ; Costa, L. E. V. L.. Simulação Computacional de Bobinagem Filamentar Não-Geodésica de Vaso de Pressão de Motor Foguete. Journal of Aerospace Technology and Management (Online), v. 01, p. 185-191, 2009.

Ho, S. Y. Structural Failure Analysis and Prediction Methods for Aerospace Vehicles and Structures, Bentham Science Publishers, 2010.

Moura, G. S. Desenvolvimento de um Estato-Reator a Combustão Supersônica. 25f. Proposta de Tese (Doutorado em Ciência, Engenharia Mecânica e Aeronáutica) – Instituto Tecnológico de Aeronáutica, São José dos Campos, 2009.

Reddy, J. N. and Gartling, D. K. The Finite Element Method in Heat Transfer and Fluid Dynamics, Ed. 3, CRC Press, Taylor & Francis Group, Boca Raton, 2010.

Rolim, T. C. Experimental Analysis of a Hypersonic Waverider. 2009. 120 f. Tese (Mestrado em Ciência, Engenharia Mecânica e Aeronáutica) - Instituto Tecnológico de Aeronáutica, São José dos Campos, 2009.

Rolim, T. C., Minucci, M. A. S., Toro, P. G. P., and Soviero, P. A. O., 2009, Experimental Results of a Mach 10 Conical-Flow Derived Waverider. 16th AIAA/DLR/DGLR International Space Planes and Hypersonic Systems and Technologies Conference. AIAA 2009-7433.

Rolim, T.C., Toro, P.G.P., Minucci, M.A.S, Oliveira, A.C., Follador, R.C., 2011, Experimental results of a Mach 10 conical-flow derived waverider to 14-X hypersonic aerospace vehicle. Journal of Aerospace Technology and Management, São José dos Campos, Vol.3, No.2, pp. 127-136, May-Aug.

Thornton, E. A. Thermal Structures for Aerospace Applications. AIAA Education Series, J.S. Przemieniecki, Series Editor-in-Chief, 1996, AIAA, ISBN 1-56347-190-6.

7. AUTHORIAL RESPONSIBILITY

"The authors are the unique responsible for the content of this work".